Biosensors and Bioelectronics 212 (2022) 114434

Contents lists available at ScienceDirect

Biosensors and Bioelectronics

journal homepage: www.elsevier.com/locate/bios

Qualitative and quantitative detection of microcystin-LR based on SERS-FET dual-mode biosensor

Meng Tian [a], Jihua Wang [b], Chonghui Li [b], Zhenxing Wang [b], Guofeng Liu [b], Enguang Lv [b], Xiaofei Zhao [a], Zhen Li [a], Dongyan Cao [b], Huilan Liu [b], Chao Zhang [a,*], Shicai Xu [b,**], Baoyuan Man [a,***]

[a] School of Physics and Electronics, Shandong Normal University, Jinan, 250014, China
[b] Shandong Key Laboratory of Biophysics, Institute of Biophysics, Dezhou University, Dezhou, 253023, China

ARTICLE INFO

Keywords:
SERS
AuNPs-modified G-FET biosensor
Microcystin-LR
Aptamer

ABSTRACT

Microcystin-LR (MC-LR), a kind of hepatoxin produced by cyanobacteria blooms, can promote liver cancer through long-term exposure even at low concentrations. In this study, a novel biosensor based on surface-enhanced Raman scattering (SERS) and field effect transistor (FET) dual sensing mode was developed by using gold nanoparticles (AuNPs)/graphene composite as sensing material. Based on the SERS sensing mode, the Raman fingerprint spectrum of MC-LR was obtained through the specific combination of MC-LR aptamer and MC-LR. The SERS enhanced effect of the AuNPs was also verified by theoretical simulation. By using FET sensing mode, the graphene field effect transistor (G-FET) biosensor respectively exhibited the detection limit as low as 0.62 aM and 0.91 aM in phosphate buffered saline (PBS) and human serum, and showed a good linear relationship in a wide range of 1×10^{-18} to 1×10^{-8} M in both solutions. Meanwhile, the sensor was utilized for the detection of MC-LR in actual water samples, and the complex components in the water did not interfere with MC-LR detection, indicating a significant high specificity of the sensor. The SERS-FET dual-mode biosensor can provide more detection options and improve the reliability of measurement results, which may has a great application prospect in the field of water environment detection.

1. Introduction

Microcystins (MCs) are a kind of cyclic heptapeptide compound with biological activity, which is the most widely distributed hepatic toxin (Kordasht et al., 2020; Chen et al., 2016). It is mainly produced by the fresh water algae microcystis aeruginosa, and has considerable stability due to the ring structure and spacer double bond in MCs. MCs can be divided into MC-LR, MC-RR, MC-YR and other types (L, R, Y represent leucine, arginine and tyrosine, respectively). MC-LR has been extensively studied due to its greater toxicity than other isomers in MCs. As a common toxin, it can strongly inhibit the activity of protein phosphatase and lead to liver tumor disease. MC-LR pollution can also cause poisoning and death of wild animals, livestock and poultry, which has become a hot topic of international public health scientists and biologists (Li et al., 2019). The national standard for Drinking Water Quality of the People's Republic of China (GB 5749-2006) allows the concentration of MC in drinking water to be less than 1 μg/L, and the implementation of this standard puts forward higher requirements for the quality of water sources (World Health Organization, 1996). Therefore, exploring a new method for trace detection of MC-LR has become an urgent need in the field of water environmental monitoring. Methods for the detection of MC-LR have been widely developed, such as bioassay (Liu et al., 2021), cytotoxicity assay (Ma et al., 2018), enzyme-linked immunosorbent assay (ELISA) (H. Zhang et al., 2022), high performance liquid chromatography (HPLC) (Aguete et al., 2003), capillary electrophoresis (CE) (Yan et al., 2019) and protein phosphatase inhibition (Mash and Wittkorn, 2016). However, these methods suffer from varying degrees of defects, such as time-consuming, cumbersome operation, low sensitivity, and most importantly, inability to distinguish the isomers of MC-LR.

* Corresponding author.
** Corresponding author.
*** Corresponding author.
E-mail addresses: czsdnu@126.com (C. Zhang), shicaixu@dzu.edu.cn (S. Xu), byman@sdnu.edu.cn (B. Man).

https://doi.org/10.1016/j.bios.2022.114434
Received 26 April 2022; Received in revised form 25 May 2022; Accepted 26 May 2022
Available online 28 May 2022

Currently, many efforts have been made in the development of single biosensor to achieve highly specificity detection of biomolecules. However, this specificity is highly susceptible to interference from other molecules in the complex system sample, thus affecting the sensitivity of the target molecule. To improve the sensitivity and reliability of sensor detection system, it is necessary to develop a dual-mode sensor with complementary advantages. The combination of surface-enhanced Raman scattering (SERS) and field effect transistor (FET) is a good choice to improve the sensitivity and reliability. In recently, SERS and FET have been aroused public concern since they are easy to operate, integrated and can provide label-free, high stability, high specificity and high sensitivity detection for some biological small molecules. SERS is a fingerprint spectroscopy technology with high specificity, which can distinguish different molecules by unique molecular vibration mode (Lee et al., 2018; Berus et al., 2021). SERS mainly utilizes the local electromagnetic field enhancement caused by the surface plasmon resonance (SPR) of the rough noble metal (e.g. Au, Ag, Cu) to increase the Raman signal. At present, it has been widely used in surface science (Hao et al., 2018), biomedicine (Li et al., 2021; Li et al., 2020), drug analysis (Fei et al., 2017; C. Zhang et al., 2020), food safety (Xie et al., 2022) and environmental monitoring (X. Zhang et al., 2020). However, SERS still has some challenges for the quantitative detection of some molecules. In contrast, the FET exploits the electric field effect to control its current, exists a certain advantage for quantitative detection of molecules. Moreover, the outstanding performance of FET is that it can analyze the interaction state of biomolecules by establishing a molecular interaction dynamics model to realize trace detection of biomolecules (Xu et al., 2017), which paves a new way to improve the reliability of sensitivity in the field of sensors.

Herein, a sensitive and label-free SERS-FET dual sensing mode was proposed for qualitative and quantitative analysis of MC-LR. Using glass patterned with source and drain electrode as the supporting substrate, monolayer gold nanoparticles (AuNPs) and graphene were transferred to the surface of glass in sequence as sensing channels to form the graphene field effect transistor (G-FET). MC-LR aptamer as probes was modified on the AuNPs/graphene surface by the bonding of Au–S to specifically capture MC-LR. SERS spectrum of MC-LR based on AuNPs/graphene/glass substrate also can be obtained, and the SERS sensing mode shows good sensitivity and high specificity to MC-LR. The G-FET sensing mode is more convenient sensitive to detect low concentrations of MC-LR due to electron transfer between graphene and AuNPs by applying a voltage. The low detection limit and affinity constant K_a were obtained in both phosphate buffered saline (PBS) or serum system. The sensor was also applied in the detection of the real water samples, and the recovery rate reached 92.59%–106.94%, which proved the practicality and strong anti-interference ability of the sensor. The combination of SERS and FET provided more options for MC-LR detection and realized the qualitative and quantitative analysis of MC-LR, which had broad application prospects in early water environment safety monitoring.

2. Experiment section

2.1. Materials and reagent

Chloroauric acid ($HAuCl_4 \bullet 4H_2O$, 99.999%), trisodium citrate dihydrate ($C_6H_5Na_3O_7 \bullet 2H_2O$, ≥99%), microcystin-LR (MC-LR), microcystin-RR (MC-RR) were obtained from Sigma-Aldrich (USA). Tannic acid ($C_{76}H_{52}O_{46}$), n-hexane (97%) and potassium carbonate (K_2CO_3, ≥99%) were supplied from Sinopharm Chemical Reagent Co., Ltd. (China). Bovine serum albumin (BSA) and human serum were purchased from Abcam Co., Ltd. (Shanghai, China). The aptamer of MC-LR with the sequences of 5′–SHC_6–GGCGCCAAACAGGACCACCATGACAATTACCCATACCACCTC-ATTATGCCCCATCTCCGC-3’ (60 nt) was synthesized by Shanghai Sangon Biotechnology Co., Ltd., (Shanghai, China). Deionized water (DI water) and tap water were taken from the laboratory and the fresh lake water was collected from a reservoir near the city of Dezhou, and they were stored in brown bottles at 4 °C.

2.2. Apparatus

The morphology of the samples was characterized by scanning electron microscope (SEM ZEISS Gemini SUPRA55). Raman spectrometer (Horiba HR Evolution 800) with laser wavelength of 633 nm was used to collect the SERS spectrum of the samples. The laser excitation energy was set at 5% of 14 mW and the spot size is 1 μm. The experiment was carried out under the diffraction grid of 1200 gr/mm^{-1} and 50 times objective lens, and using an integration time of 4 s. The morphology and size of AuNPs were characterized using a high-resolution transmission electron microscope (HRTEM, JEOL-2100F). Ultraviolet–visible (UV–vis) spectroscopy (UV2600, SHIMADZU CORPORATION) was applied to study the absorption peak of the AuNPs. The hydrodynamic diameters and zeta potential of the AuNPs were obtained using a dynamic light scattering (DLS, Zetasizer Nano ZS).

2.3. Preparation of AuNPs solution

The AuNPs were synthesized by a simple hydrothermal reduction method. An 80 mL aqueous solution containing 5 mL 0.002 g/mL $HAuCl_4$ and 75 mL DI water was placed in a round-bottomed flask, which was heated at 60 °C under magnetic stirring. And then 1.36×10^{-4} mol $C_6H_5Na_3O_7 \bullet 2H_2O$, 5.87×10^{-7} mol $C_{76}H_{52}O_{46}$, 5.06×10^{-6} mol K_2CO_3 were dissolved in DI water under ultrasound and quickly added to the round-bottomed flask and mixed with the $HAuCl_4$ aqueous solution, which was maintained for 1 h. The color changed from light yellow to wine red, then AuNPs solution was formed. The AuNPs solution was washed with DI water and centrifuged for three times (12000 rpm/min, 30 min).

2.4. Self-assembly of AuNPs and fabrication of the substrate

The self-assembled process of AuNPs and fabrication of the substrates layer-by-layer was shown in Fig. 1. 20 mL AuNPs solution was added to the plate with the diameter of 90 mm using a pipette gun and 20 mL n-hexane was transferred subsequently to the upper surface of the AuNPs solution to form an oil/water interface (Fig. 1A–B). Next, ethanol solution was slowly introduced to AuNPs/n-hexane solution using a syringe, a AuNPs layer was formed at the oil/water interface (Fig. 1C–D). This phenomenon can be interpreted that the substitution of Au-chloride ions by ethanol molecules to reduce the surface charge of the AuNPs/n-hexane solution, thus leading to an array of AuNPs at the oil/water interface (Si et al., 2016; Zhao et al., 2018).

The glass substrate patterned with indium tin oxide (ITO) electrode was washed by acetone, ethanol and DI water. The graphene was fabricated by chemical vapor deposition (CVD) on Cu sheet as described in previous work (Tian et al., 2020). The graphene film was transferred to an ITO/glass substrate by wet transfer (Kim et al., 2009). Next, the graphene/ITO/glass substrate was immersed into the mixture solution to pick up the formed AuNPs film at the oil/water interface (Fig. 1E). Graphene and the AuNPs film are tightly combined due to electrostatic adsorption.

2.5. Aptamer immobilization on AuNPs/graphene/glass substrate and detection of MC-LR

In order to perform biological functionalization on the G-FET channel surface, the 200 nM MC-LR aptamer with sulfhydryl group (SH-) was modified at the AuNPs/graphene surface using Au–S bonding at room temperature (Fig. 2A–B). To prevent the occurrence of non-specific binding, 100 mM ethanolamine was introduced into the G-FET sensor channel to encapsulate unbound sites on the AuNPs/graphene surface (Fig. 2C). Finally, different concentrations of MC-LR in range of 1 ×

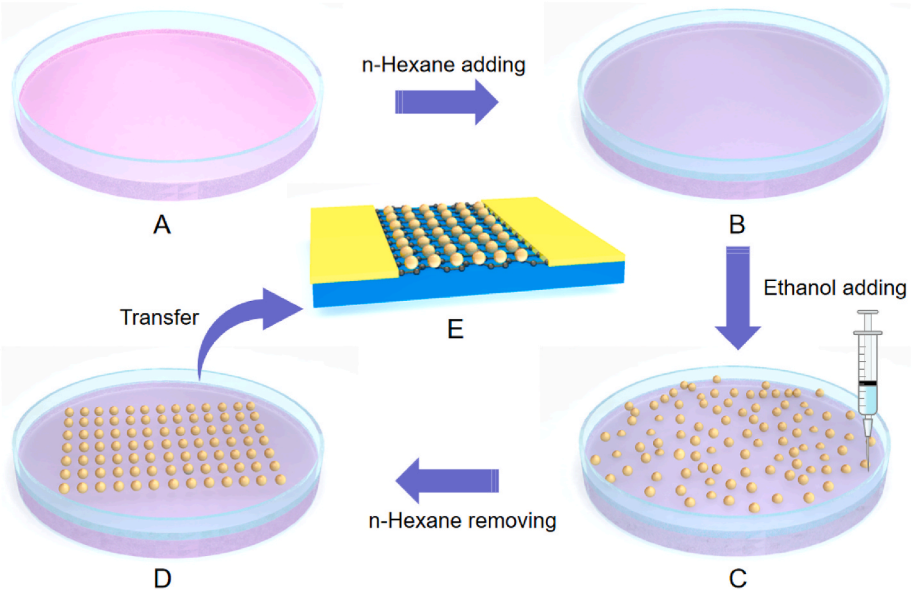

Fig. 1. Schematic illustration of the self-assembly process of AuNPs on the graphene/ITO/glass substrate.

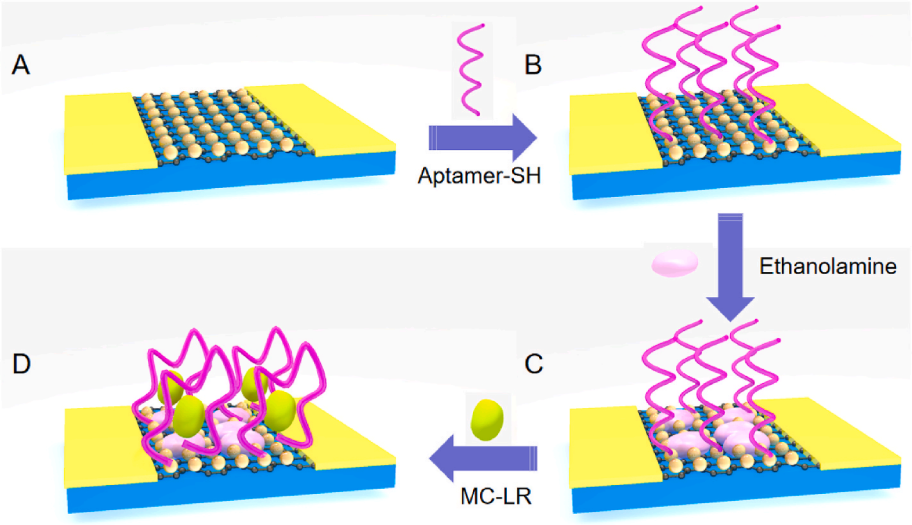

Fig. 2. Process of immobilization of MC-LR aptamer onto AuNPs/graphene/glass substrate and detection of MC-LR.

10^{-18} to 1×10^{-8} M was gradually introduced into the channel of G-FET for trace detection of MC-LR (Fig. 2D).

3. Results and discussion

3.1. Characterization of AuNPs/graphene

The SEM images in Fig. 3A and B show the surface morphology of the self-assembled AuNPs. It was clearly observed that the AuNPs were uniform in size and formed a dense monolayer with low porosity. The nanoscale gaps between AuNPs and AuNPs were achieved, which are expected to have excellent Raman enhancement effect. A large area AuNPs nano-film on the oil/water interface was obtained (see the inset in Fig. 3A). The continuity and integrity of Au films indicate that AuNPs nano-film is of good quality. The TEM images of AuNPs are shown in Fig. 3C, it can be found that the AuNPs are homogeneous and the average sizes are approximately 15.04 nm (Fig. 3E). The selected area electron diffraction (SAED) pattern of single AuNPs in Fig. 3D indicates that the AuNPs are polycrystalline, which can be attributed to (111), (200), (220) and (311) diffraction rings of AuNPs. To demonstrate the hydrophilicity of AuNPs, dynamic light scattering (DLS) measurement was performed on AuNPs solutions, and the average particle sizes of AuNPs are about 28.01 nm (Fig. 3F). The particle size measured by DLS is larger than TEM due to the surface of AuNPs is wrapped with a layer of water, which proves that AuNPs have good hydrophilicity and is suitable for the detection of biomolecules.

3.2. Plasmonic performance and SERS measurements of MC-LR

The absorption of AuNPs/graphene, aptamer/AuNPs/graphene and MC-LR/aptamer/AuNPs/graphene was characterized by UV–vis absorption spectra in Fig. 4A. The absorption band of aptamer/AuNPs/graphene, MC-LR/aptamer/AuNPs/graphene successively shifted to red light direction. The red shift of the absorption band can be attributed to the addition of the aptamer and MC-LR (He et al., 2018). As the absorption bands of the samples are in the range from 651 to 668 nm, a 633 nm laser source with 5% of 14 mW was used for Raman excitation. Generally, the enhancement of Raman signal is attributed to the

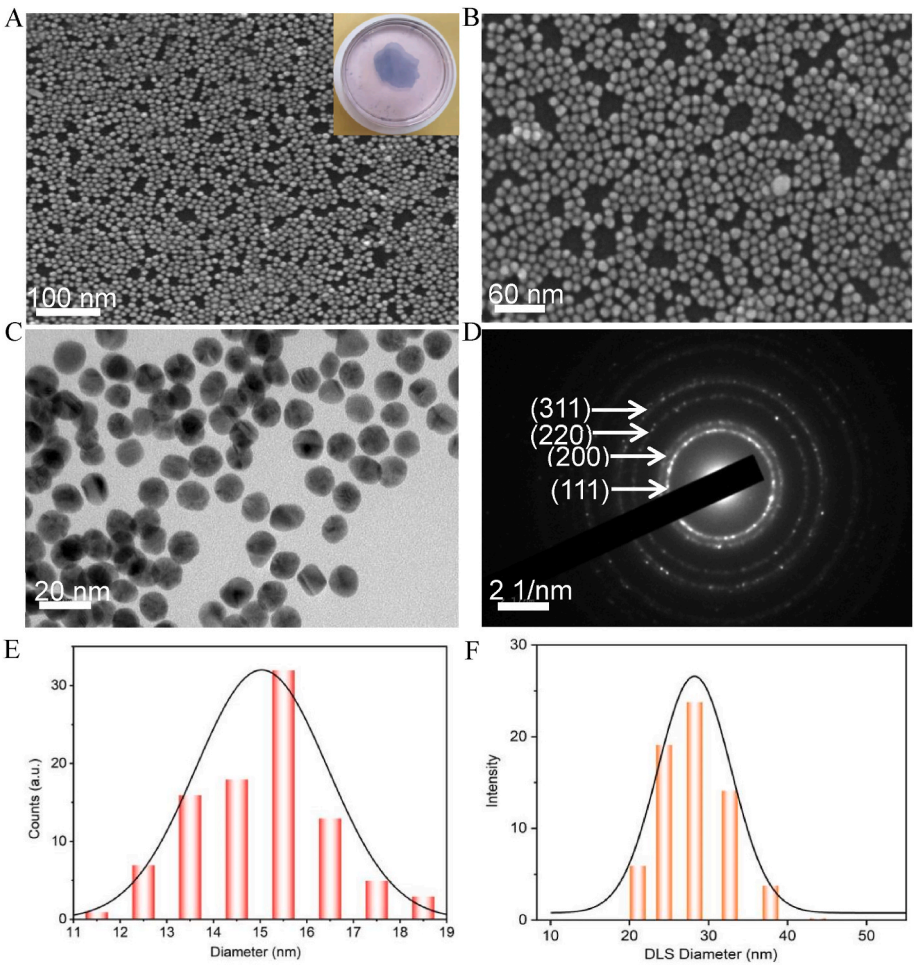

Fig. 3. (A) Low and (B) high-magnification SEM images of AuNPs. The inset shows the photo of the monolayer AuNPs film on the oil/water interface. (C) TEM images of the AuNPs. (D) SAED pattern of the AuNPs. (E) size and (F) DLS diameter distributions of AuNPs.

enhancement of the local electromagnetic field caused by local surface plasmon resonance (LSPR) of noble metal (e.g. Au, Ag, Cu) (Bharati and Soma, 2021; Zhao et al., 2021). The AuNPs can generate strong LSPR effect under laser excitation at 633 nm and greatly enhance the intensity of Raman spectrum. Moreover, the AuNPs have excellent stability and biocompatibility and are suitable for biological detection (Y. Zhang et al., 2022; Mahmoudpour et al., 2021). The SERS measurement result of MC-LR is shown in Fig. 4B, and the SERS spectroscopy provides unique "fingerprint" information of MC-LR on AuNPs/graphene/glass substrate, such as primary characteristic Raman shifts of 640, 748, 757, 845, 889, 975, 1019, 1188, 1211, 1267, 1294, 1310, 1382, 1458, 1493, 1530, 1581 cm^{-1}. The change of Raman shifts can be attribute to the vibration modes of MC-LR and detailed in Table 1, which indicates that the MC-LR molecules were captured by specific binding of MC-LR aptamer on the AuNPs surface. To further verify the SERS effect of AuNPs, we calculated the local electric field distribution of AuNPs using the finite-different time-domain (FDTD) theory simulation (Fig. 4C–D). As shown in Fig. 4C, the area marked with red circle on the SEM image was chosen to simulate. The diameter of AuNPs was set as 15 nm and all the gaps between the AuNPs were set as 0.5 nm. The laser wavelength of 633 nm was selected in the simulation. Fig. 4D shows that the dense hot spots mainly distribute in nanogaps between the AuNPs. An electric field magnification of 23.699 times was obtained by calculation. Thus, the enhancement of SERS signals can be attributed to the strong electric fields.

3.3. Electrical characterization of the G-FET sensor

Fig. 5A illustrates the transfer characteristic curve of the G-FET and the one after AuNPs modified graphene surface. The deposition of AuNPs causes the left shift of the transfer characteristic curve of the G-FET sensor, inducing n-type doping on graphene surface. The n-type doping of the AuNPs can be explained that the work function of graphene is smaller than that of Au, which leads to the transfer of electrons from AuNPs to graphene (Wang et al., 2020). As shown in Fig. 5B, the electron transport can be modulated by gate voltage (V_{gs}), showing the typical field effect characteristics. Moreover, the drain-source current (I_{ds}) and drain-source voltage (V_{ds}) have a linear relationship, indicating that good ohmic contact between AuNPs/graphene and source-drain electrode. The electrical characteristics of G-FET sensor were measured to verify the performance of the sensor. To obtain a clean graphene sensing interface, the device needs to be current annealed before measurement using a semiconductor parameter analyzer system (PDA FS360) with the probe table (PEH-4) (Fig. 5C). After more than ten rounds of gate voltage sweeps, the transfer characteristic curve and the charge neutral point (V_{CNP}, i.e. Dirac point) are not changing again, indicating that the electrical properties of the G-FET device have been stabilized and can be used as biosensors (Kireev et al., 2017). The transfer characteristic curves of the G-FET are further shifted to the left direction after add to aptamer and ethanolamine solution in Fig. 5D. The addition of the thiol-modified 200 nM aptamer results in a large left shift of the V_{CNP} to about 47 mV. It can be explained that the negative charge of the aptamer in PBS 7.4 produces n-type doping to graphene. To

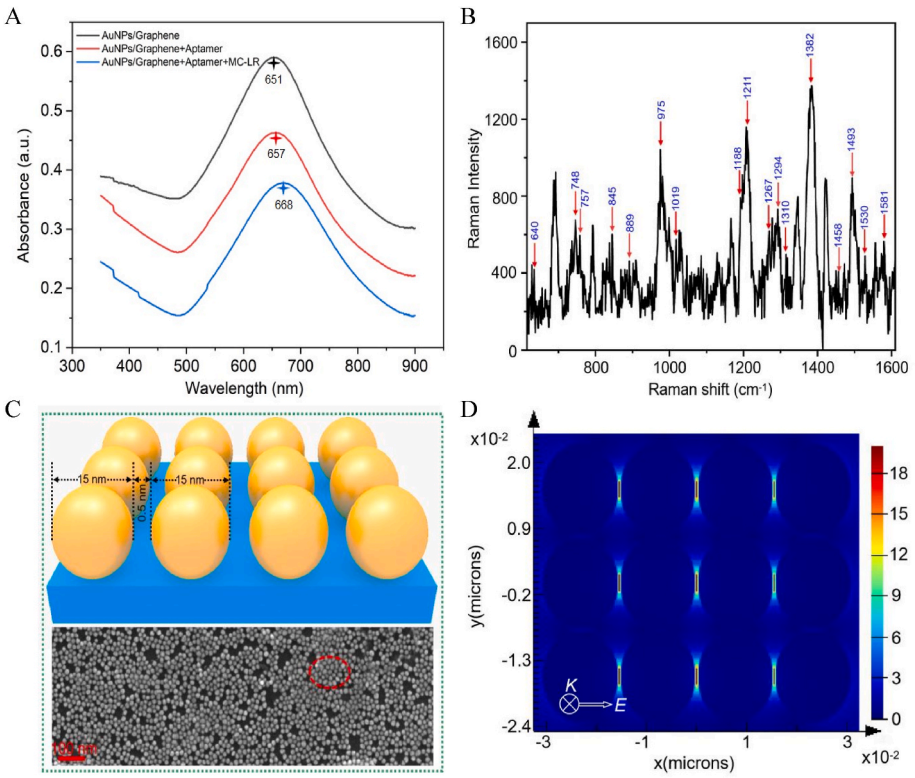

Fig. 4. (A) UV–vis absorption spectra of AuNPs/graphene, aptamer/AuNPs/graphene and MC-LR/aptamer/AuNPs/graphene. (B) SERS spectrum of MC-LR on AuNPs/graphene/glass substrate. (C) Schematics of the FDTD theoretical simulation and the local SEM images of the AuNPs. (D) The local electric field distribution of the AuNPs on the substrate with x-y cross-section.

Table 1
Band assignments for Raman spectrum of MC-LR.

Raman shift (cm^{-1})	molecular vibration mode (He et al., 2019; Hassanain et al., 2017; Halvorson and Vikesland, 2011)
640	C–C twisting , COO^- wagging
748, 757	COO^- bending, C–H out-of-plane bending, CH_2 rocking
845	C–C stretch, CH_2 rocking, CH_3 rocking
889	CH_2 rocking, C–COO^- stretch
975	ν(C–C) wagging, p(CH3), δ(CCH)
1019	C–H bending in plane, C–N stretch
1188	NH_3^+ rocking
1211	phenyl ring vibrations, CH_2 twisting
1267, 1294	NH_3^+ rocking, amide III vibrations
1310	CH2 twisting, Cα-H bending, H-Cα-Cterminal vibrations, amide III vibrations, C–H bending in plane
1382	CH vibrations
1458	C–H bending, CH_2 scissoring, CH_3 asymmetric bending
1493	NH_3^+ symmetric bending
1530	Amide II vibration modes
1581	C–C stretching, COO^- stretch

prevent non-specific adsorption of interfering substances, 100 mM ethanolamine was added to block the unbound aptamer of the G-FET (Danielsona et al., 2020; Song et al., 2022).

3.4. High affinity and selectivity of the G-FET sensor in PBS and human serum

To evaluate the performance of the G-FET sensor, the concentration of MC-LR in PBS was measured. The MC-LR solutions with the concentrations from 1×10^{-18} to 1×10^{-8} M were sequentially introduced into the sensor. The V_{CNP} of the G-FET sensor gradually shifts to the right with increasing concentration of MC-LR (Fig. 6A). In general, the minimum detection limit of a sensor was estimated by 3 times the standard deviation (3σ) of the sensor responses to blank solution (Liu et al., 2011; Chen et al., 2022). Here, the G-FET sensor shows a very low detection limit of about 0.62 aM. The low detection limit of the sensor can be attributed to the high surface-to-volume ratio of AuNPs/graphene composite, as well as the doping effect caused by the AuNPs. The AuNPs significantly induce charge doping on graphene and increase the carrier concentration of graphene (J. Li et al., 2021; Shin et al., 2021). The study of the interaction affinity between the aptamer and MC-LR is particularly important for the sensitivity of the sensor. Therefore, the equilibrium association constant (K_a) and comprehensive coordination number (n) are calculated by the following equations (1)–(5). The interaction between aptamer and MC-LR can be expressed by equation. (1)

$$n[MC-LR]+[apt] \xrightarrow{binding} [MC-LR]\times[apt] \quad (1)$$

[MC-LR] and [apt] represent the concentration of MC-LR and aptamer, respectively. As in equation. (2), K_a can be calculated.

$$Ka = \frac{[MC-LR]\times[apt]}{[MC-LR]^n \times [apt]} \quad (2)$$

Take the logarithm of equation. (2) to get equation. (3).

$$\lg \frac{[MC-LR]\times[apt]}{[apt]} = n\lg[MC-LR] + \lg Ka \quad (3)$$

According to Lambert-Beer law, the$\triangle V_{CNP}$ is proportional to the concentration of the MC-LR in Fig. 6B.

Then,

$$\lg \frac{[MC0-MCx]}{[MCx-MC1]} = n\lg[MC-LR] + \lg Ka \quad (4)$$

Where MC_0 is the V_{CNP} of G-FET before adding MC-LR. MC_x is the V_{CNP} after adding x M of MC-LR and MC_1 is the maximum concentration of

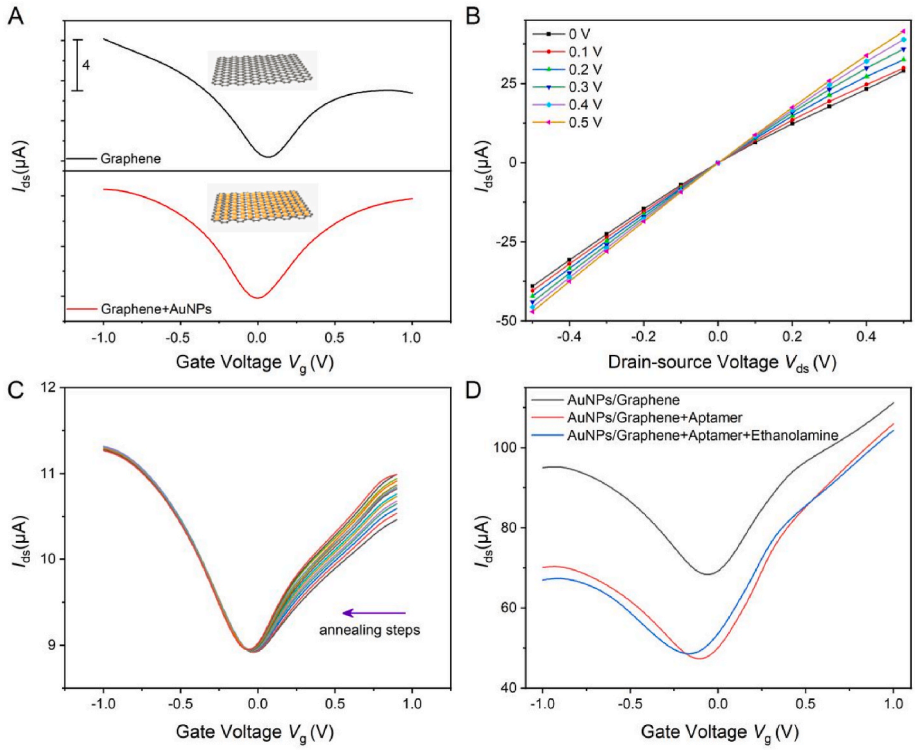

Fig. 5. (A) Electrical response of the sensor before and after modification by AuNPs. (B) Transfer output curves of AuNPs-modified G-FET I_{ds} versus V_{ds} with the variation V_{gs} from −1.0 to 1.0 V. (C) Effect of the current annealing of AuNPs-modified G-FET sensor before detection of MC-LR. (D) Transfer characteristic curves of the G-FET sensor at each functionalization step.

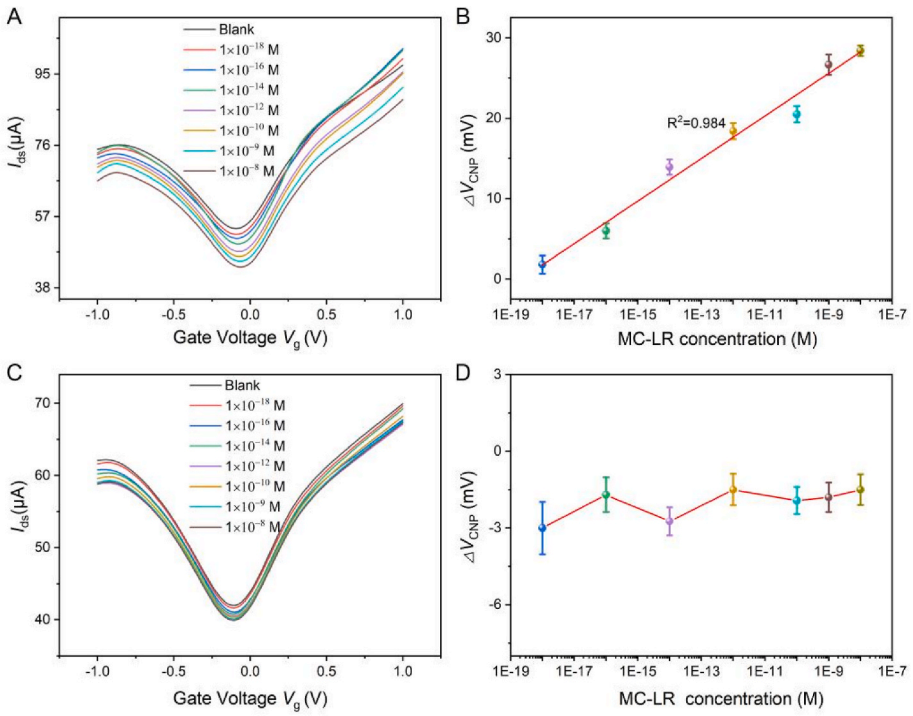

Fig. 6. (A) Transfer characteristics of the G-FET biosensor with MC-LR aptamer exposed to MC-LR in PBS buffer from 1×10^{-18} to 1×10^{-8} M. (B) Linear plot characteristics of $\triangle V_{CNP}$ of sensor versus the concentration of MC-LR in PBS buffer. (C) Transfer characteristics of the G-FET biosensor in the absence of MC-LR aptamer to detect MC-LR from 1×10^{-18} to 1×10^{-8} M. (D) The $\triangle V_{CNP}$ versus the concentration of MC-LR of the G-FET biosensor without MC-LR aptamer. Error bars represent the relative standard deviation (RSD) of four measurements for each concentration.

MC-LR.

Finally, equation. (4) can be simplified to equation. (5)

$$y = n\lg[MC - LR] + \lg Ka \quad (5)$$

Thus, the value of K_a is as high as 7.07×10^5 and n is 2.64 calculated by y = 2.64x + 5.85 (Fig. 6B). The order of magnitude of K_a and n are similar to the previous literature as 2.317×10^6 and 1.006, respectively (Ke et al., 2014). The high affinity between MC-LR and aptamer indicates that the selected aptamer is suitable for MC-LR detection and expected to obtain the sensor with high specificity. Moreover, in order to test the inertness of AuNPs/graphene to MC-LR, a control experiment was performed. The G-FET sensor was exposed to different

concentrations of MC-LR in the absence of aptamer (Fig. 6C–D). The shift of the V_{CNP} is negligible (<3 mV), which shows that the G-FET sensor is suitable for the detection of MC-LR with high stability.

The specificity of the G-FET sensor on MC-LR was further measured by performing electrical detection in bovine serum albumin (BSA), MC-RR and MC-LR. The electrical response of the G-FET sensor induced by MC-LR is significantly higher than that of BSA and MC-RR at the same concentration of 100 nM as shown in Fig. 7A and B. The excellent specificity of this sensor is mainly attributed to the high affinity between the aptamer and MC-LR. To confirm the feasibility of MC-LR detection in complex components, the G-FET sensor was performed in human serum. As shown in the Fig. 7C, the shift in V_{CNP} was closely related to the concentration of the MC-LR in human serum. With the increase of the concentration of the MC-LR, the V_{CNP} of the G-FET sensor gradually shifted to the left direction. The $\triangle V_{CNP}$ and the concentration logarithmic diagram of the MC-LR show a good linear dependence, showing excellent sensing performance in serum. In addition, we also notice that with the increase of MC-LR concentration, the V_{CNP} in human serum and in PBS shifted to opposite direction. This can be explained that the MC-LR shows opposite charge. In contrast in PBS, the MC-LR in serum is negatively charged which caused the V_{CNP} shift to the left direction. According to equations (1)–(5), the affinity and comprehensive coordination number (n) between MC-LR and aptamer can be calculated as $K_a = 1.41 \times 10^6$ and n = 1.12 (Fig. 7D). The low detection limit of the G-FET in serum for MC-LR detection is down to 0.91 aM, showing that the G-FET can be used for trace MC-LR detection in serum. We also performed the control experiment to detect different concentrations of MC-LR in the absence of aptamer (Fig. 7E–F). In that case, the shift of V_{cnp} was also negligible for MC-LR measurement in the complex system of human serum. The small response signal of the G-FET sensor can be attributed to the slight non-specific adsorption of MC-LR.

3.5. Analysis of the MC-LR in real water samples

Compared to buffers and serums, real water samples are very complex systems, containing many interfering molecules, such as biopesticides, bioherbicides, insecticides, internal secretions and bioproductivity agents. To evaluate the suitability and practical application ability of the developed G-FET biosensor for the detection of MC-LR by the standard addition method. We selected DI water, tap water and fresh lake water filtered by centrifugation as real water samples, and the low concentration MC-LR was added into these three water samples. Each water sample was prepared with the MC-LR concentration of 50 pM, 100 pM and 175 pM, respectively. The developed G-FET sensor exhibit a high detection rate for the three samples as shown in the Table 2. It obtained a good recovery of 92.59%–106.94% and the standard deviation was ranging from 4.3% to 12.8% respectively in DI water, tap water and fresh lake water, demonstrating a high sensitivity

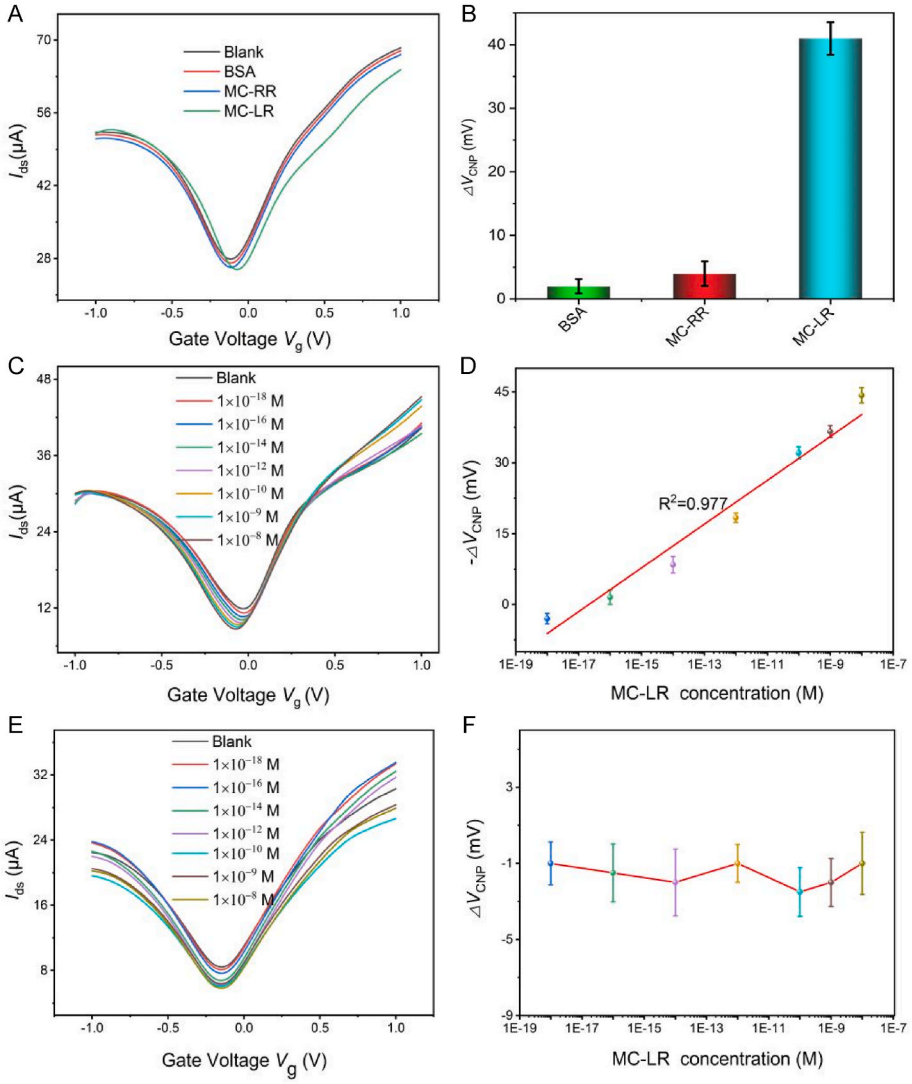

Fig. 7. (A) Transfer characteristic curves of the G-FET sensor in the presence of 100 nM BSA, 100 nM MC-RR and 100 nM MC-LR. (B) The $\triangle V_{CNP}$ of the G-FET sensor to BSA, MC-RR and MC-LR. (C) Transfer characteristic curves of the G-FET sensor in the presence of MC-LR aptamer for MC-LR detection in human serum at different concentrations from 1×10^{-18} to 1×10^{-8} M. (D) Linear plot characteristics of $\triangle V_{CNP}$ of sensor versus the concentration of MC-LR in human serum. (E) Transfer characteristic curves of the G-FET sensor in the absence of MC-LR aptamer for MC-LR detection in human serum at different concentrations from 1×10^{-18} to 1×10^{-8} M. (F) The $\triangle V_{CNP}$ of G-FET sensor without MC-LR aptamer. Error bars represent the RSD of four measurements for each concentration.

Table 2
Detection of the MC-LR in real water samples by the G-FET sensor.

Sample	G-FET Measured (pM)	RSD (%)	Recovery (%)
DI water + MC-LR[a] 1	53.19	5.4	106.38
DI water + MC-LR[b] 2	95.23	4.3	95.23
DI water + MC-LR[c] 3	178.57	9.7	102.04
Tap water + MC-LR[a] 1	52.91	10.8	105.82
Tap water + MC-LR[b] 2	92.59	6.3	92.59
Tap water + MC-LR[c] 3	166.66	7.5	95.23
Fresh lake water + MC-LR[a] 1	53.47	8.7	106.94
Fresh lake water + MC-LR[b] 2	98.03	7.8	98.03
Fresh lake water + MC-LR[c] 3	172.41	12.8	98.52

RSD is the relative standard deviation.
[a] 50 pM MC-LR was added to the DI water, tap water and fresh lake water, respectively.
[b] 100 pM MC-LR was added to the DI water, tap water and fresh lake water, respectively.
[c] 175 pM MC-LR was added to the DI water, tap water and fresh lake water, respectively.

and accuracy of the G-FET sensor in the quantitative determination of MC-LR. Moreover, the RSD of measured values of the MC-LR is very low no matter in DI water, tap water and fresh lake water, indicating that the G-FET show high stability (Fig. 8).

4. Conclusion

In summary, by self-assembly AuNPs on graphene surface, we developed a novel, simple and label-free SERS-FET dual-mode sensor to achieve highly sensitive and specific detection of MC-LR. The SERS fingerprint spectrum of MC-LR was obtained on the AuNPs/graphene/glass substrate, indicating that SERS sensor can be used for specific qualitative detection of MC-LR. The quantitative detection of MC-LR was achieved by the G-FET sensing mode with a detection limit as low as 0.62 aM and 0.91 aM in PBS buffer and human serum, respectively. In addition, the feasibility of the G-FET sensor was verified by detecting MC-LR in real samples. The presence of other interference signals in complex serum and water environment do not obviously affect the measurement of MC-LR due to the good specificity of the sensor. The studies have shown that the high sensitivity and high specificity of the G-FET sensor from the high affinity of MC-LR and aptamer. The combination of SERS and FET sensing mode realized the qualitative and quantitative detection of MC-LR, which may have a promising application prospect in water environment detection.

CRediT authorship contribution statement

Meng Tian: Writing – original draft, Conducting the experiments and writing the paper, Synthesizing the gold nanoparticles, making the sensors and operating the semiconductor parameter analyzer. **Jihua Wang:** Formal analysis, Analyzing the data and modifying the paper, All authors discussed, read and approved the final manuscript. **Chonghui Li:** Preparing graphene by CVD. **Zhenxing Wang:** Performing SEM. **Guofeng Liu:** Performing SEM, and. **Enguang Lv:** Performing SEM. **Xiaofei Zhao:** Performing Raman spectroscopy, and. **Zhen Li:** Performing Raman spectroscopy. **Dongyan Cao:** Synthesizing the gold nanoparticles, making the sensors and operating the semiconductor parameter analyzer, and. **Huilan Liu:** Synthesizing the gold nanoparticles, making the sensors and operating the semiconductor parameter analyzer. **Chao Zhang:** Conceiving and designing this work, Formal analysis, Analyzing the data and modifying the paper, and. **Shicai Xu:** Conceiving and designing this work, Formal analysis, Analyzing the data and modifying the paper. **Baoyuan Man:** Conceiving and designing this work, Formal analysis, Analyzing the data and modifying the paper.

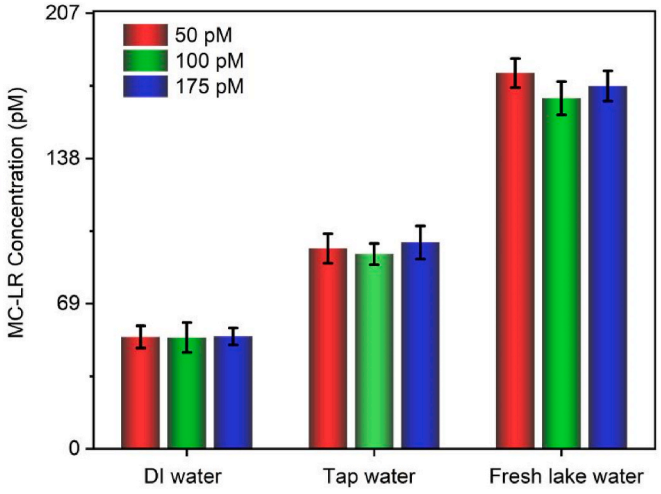

Fig. 8. The quantitative detection of MC-LR in DI water, tap water and fresh lake water by the G-FET sensor. Error bars represent the RSD of four measurements for each concentration.

Declaration of competing interest

The authors declare that they have no known competing financial interests or personal relationships that could have appeared to influence the work reported in this paper.

Acknowledgments

We are grateful for financial support from the National Natural Science Foundation of China (11974222, 62071085, 12174229, 11804200, 12004226, 12104085 and 22104011), the Taishan Scholars Program of Shandong Province (tsqn201812104), the Qingchuang Science and Technology Plan of Shandong Province (2019KJJ017, 2021KJ006), Natural Science Foundation of Shandong Province (ZR2021QA008, ZR2021QF146, ZR2021QA063 and ZR2021QB130) and China Postdoctoral Science Foundation (2019M662423).

References

Aguete, E.C., Gago-Martınez, A., Leao, J.M., Rodrıguez-Vázquez, J.A., Menàrd, C., Lawrence, J.F., 2003. Talanta 59, 697–705.
Berus, S.M., Adamczyk-Popławska, M., Młynarczyk-Bonikowska, B., Witkowska, E., Szymborski, T., Waluk, J., Kamińska, A., 2021. Biosens. Bioelectron. 189, 113358.
Bharati, M.S.S., Soma, V.R., 2021. Opto-Electron. Adv 4, 210048.
Chen, L., Chen, J., Zhang, X., Xie, P., 2016. J. Hazard Mater. 301, 381–399.
Chen, X., Kang, S., Ikbal, A., Zhao, Z., Pan, Y., Zuo, J., Gu, L., Wang, C., 2022. Biosens. Bioelectron. 202, 113971.
Danielsona, E., Sontakkeb, V.A., Porkovicha, A.J., Wanga, Z., Kumara, P., Ziadia, Z., Yokobayashib, Y., Sowwan, M., 2020. Sens. Actuators, B 320, 128432.
Fei, J., Wu, L., Zhang, Y., Zong, S., Wang, Z., Cui, Y., 2017. ACS Sens. 2, 773–780.
Halvorson, R.A., Vikesland, P.J., 2011. Environ. Sci. Technol. 45, 5644–5651.
Hao, Q., Li, W., Xu, H., Wang, J., Yin, Y., Wang, H., Chu, P.K., 2018. Adv. Mater. 30, 1705421.
Hassanain, W.A., Izake, E.L., Schmidt, M.S., Ayoko, G.A., 2017. Biosens. Bioelectron. 91, 664–672.
He, F., Liang, L., Zhou, S., Xie, W., He, S., Wang, Y., Tlili, C., Tong, S., Wang, D., 2018. Langmuir 34, 14825–14833.
He, S., Xie, W., Fang, S., Zhou, D., Djebbi, K., Zhang, Z., Du, J., Du, C., Wang, D., 2019. Talanta 195, 401–406.
Ke, H., Liu, M., Zhuang, L., Li, Z., Fan, L., Zhao, G., 2014. Electrochim. Acta 137, 146–153.
Kordasht, H.K., Hassanpour, S., Baradaran, B., Nosrati, R., Hashemzaei, M., Mokhtarzadeh, A., Guardia, M., 2020. Biosens. Bioelectron. 165, 112403.
Kim, K.S., Zhao, Y., Jang, H., Lee, S.Y., Kim, J.M., Kim, K.S., Ahn, J.H., Kim, P., Choi, J. Y., Hong, B.H., 2009. Nature 457, 706–710.
Kireev, D., Brambach, M., Seyock, S., Maybeck, V., Fu, W., Wolfrum, B., Offenhäusser, A., 2017. Sci. Re. 7, 1–12.
Lee, K.L., Hung, C.Y., Pan, M.Y., Wu, T.Y., Yang, S.Y., Wei, P.K., 2018. Adv. Mater. Interfac. 5, 1801064.
Li, C., Xu, S., Yu, J., Li, Z., Li, W., Wang, J., Liu, A., Man, B., Yang, S., Zhang, C., 2021. Nano Energy 81, 105585.

Li, J., Wu, D., Yu, Y., Li, T., Li, K., Xiao, M.M., Li, Y., Zhang, Z.Y., Zhang, G.J., 2021. Biosens. Bioelectron. 183, 113206.
Li, M., Paidi, S.K., Sakowski, E., Preheim, S., Barman, I., 2019. ACS Sens. 4, 1203–1210.
Li, N., Shen, F., Cai, Z., Pan, W., Yin, Y., Deng, X., Zhang, X., Machuki, J.O., Yu, Y., Yang, D., Yang, Y., Guan, M., Gao, F., 2020. Small 16, 2005511.
Liu, J., Xing, Y., Zhou, X., Chen, G.Y., Shi, H., 2021. Biosens. Bioelectron. 176, 112902.
Liu, R., Liu, X., Tang, Y., Wu, L., Hou, X., Lv, Y., 2011. Anal. Chem. 83, 2330–2336.
Ma, J., Li, Y., Wu, M., Li, X., 2018. Chemosphere 194, 773–783.
Mahmoudpour, M., Ding, S., Lyu, Z., Ebrahimi, G., Du, D., Dolatabadi, J.E.N., Torbati, M., Lin, Y., 2021. Nano Today 39, 101177.
Mash, H., Wittkorn, A., 2016. Water Res. 95, 230–239.
Shin, D., Kim, H.R., Hong, B.H., 2021. Nanoscale Adv. 3, 1404–1412.
Si, S., Liang, W., Sun, Y., Huang, J., Ma, W., Liang, Z., Jiang, L., 2016. Adv. Funct. Mater. 26, 8137–8145.
Song, S., Lee, J.U., Jeon, M.J., Kim, S., Sim, S.J., 2022. Biosens. Bioelectron. 199, 113864.
Tian, M., Li, Z., Song, R., Li, Y., Guo, C., Sha, Y., Cui, W., Xu, S., Hu, G., Wang, J., 2020. Appl. Surf. Sci. 503, 144303.
Wang, S., Hossain, M.Z., Han, T., Shinozuka, K., Suzuki, T., Kuwana, A., Kobayashi, H., 2020. ACS Omega 5, 30037-30046.
World Health Organization. 1996. 973-973.
Xie, T., Cao, Z., Li, Y., Li, Z., Zhang, F.L., Gu, Y., Han, C., Yang, G., Qu, L., 2022. Food Chem. 381, 132208.
Xu, S., Zhan, J., Man, B., Jiang, S., Yue, W., Gao, S., Guo, C., Liu, H., Li, Z., Wang, J., Zhou, Y., 2017. Nat. Commun. 8, 1–10.
Yan, P., Zhang, K., Wang, L., Tong, W., Chen, D.D., 2019. Electrophoresis 40, 2285–2293.
Zhang, C., Li, Z., Qiu, S., Lu, W., Shao, M., Ji, C., Wang, G., Zhao, X., Yu, J., Li, Z., 2020. Nanophotonics 11, 33–44.
Zhang, H., Li, B., Liu, Y., Chuan, H., Liu, Y., Xie, P., 2022. J. Hazard Mater. 424, 127406.
Zhang, X., Ong'achwa Machuki, J., Pan, W., Cai, W., Xi, Z., Shen, F., Zhang, L., Yang, Y., Gao, F., Guan, M., 2020. ACS Nano 14, 4045–4060.
Zhang, Y., Liu, Q., Liu, M., Zhang, X., Li, X., Dai, L., Meng, M., Liu, D., Yin, Y., Xi, R., 2022. Sens. Actuators, B 353, 131162.
Zhao, W., Xiao, S., Zhang, Y., Pan, D., Wen, J., Qian, X., Yang, Z., 2018. Nanoscale 10, 14220–14229.
Zhao, Y.Y., Ren, X.L., Zheng, M.L., Jin, F., Liu, J., Dong, X.Z., Zhao, Z.S., Duan, X.M., 2021. Opto-Electron. Adv 4, 200101-1.